Research Article

Formation of CdSe/CdS/ZnS–Au/SiO₂ Dual-Yolk/Shell Nanostructures through a Trojan-Type Inside-Out Etching Strategy

Ching-Mao Huang[1], Shih-Hsun Cheng[1], U-Ser Jeng[2], Chung-Shi Yang[3], and Leu-Wei Lo[1] (✉)

[1] Division of Medical Engineering, Zhunan Health Research Institutes, Zhunan, Miaoli 350

[2] Hsinchu Synchrotron Radiation Research Center, Hsinchu 300

[3] Center for Nanomedicine Researcher, Zhunan Health Research Institutes, Zhunan, Miaoli 350

ABSTRACT

In this work we report the development of a rapid and selective etching strategy to synthesize a dual-yolk/shell nanostructure consisting of semiconductor–metal hybrid nanocrystals and hollow SiO₂ for the first time. By utilizing CdSe/CdS/ZnS quantum dot (CSSQD)/SiO₂ core/shell nanoparticles as the template and aurate hydroxyl complexes $[Au(OH)_4^-]$ as the Trojan-type inside-out etching agent, rapid formation of CSSQD–Au hybrid nanocrystal dual-yolk and SiO₂ hollow shell occur during the reduction of $Au(OH)_4^-$ on CSSQD cores accompanied by localized hydroxyl-liberation from $Au(OH)_4^-$ at the interface between silica and CSSQD. Unlike surface-protected etching strategies, a selective as well as directional etching takes place from the silica internal surface and the thickness of the silica shell can be controlled by varying the etching time. Moreover, the size of attached Au nanoclusters can be tuned by subsequent light exposure. Consequently, the resulting platform offers a number of attractive features: (1) a new, directional, and rapid etching approach toward the formation of hollow silica nanostructures in solution; (2) semiconductor/metal hybrid nanocrystals as yolks within hollow silica nanospheres have been reported for the first time; and (3) the ability, through light exposure, to tune the size of the attached metal nanoclusters on the encapsulated CSSQD within the hollow silica nanospheres. Most importantly, the synthetic method has the capability of introducing additional guest species (e.g. metals) into a primary yolk (e.g. semiconductor) of hollow silica nanoparticles, potentially leading to many promising applications in fuel cells, photocatalysis, bioimaging, and cancer therapy.

1. Introduction

Yolk/shell or "rattle-type" nanostructures possess internal voids and thin shells, causing them to exhibit unique properties—low density, excellent loading capacity, large surface area, moveable cores, and high permeability—that are not possible with conventional core/shell nanoparticles (NPs) [1–3]. Yolk/shell nanomaterials have recently attracted much attention because of their potential applications as catalysts in recyclable nanoreactors [4–9], as nanomedicines in bioapplications [10–20], and as anion electrodes in

Address correspondence to lwlo@nhri.org.tw

lithium ion batteries [21, 22]. Among the known yolk/shell nanomaterials, silica-based hollow nano-spheres (*h*SiO$_2$) have drawn much attention because of their high permeability, ready surface modification, optical transparency, and biocompatibility. Based on the wide range of available silica chemistry, yolk@*h*SiO$_2$ NPs have been prepared using diverse strategies, including a sacrificial template method [23], a soft template strategy [24, 25], a template-free method [26–28], a surface-protected etching process [29–31], and a difference-based selective etching strategy [32]. To realize the concept of a yolk/shell nanoreactor, it is critical to develop the capability of introducing additional guest species (e.g. Ag, Au, Pt, Pd) into a primary yolk (e.g. semiconductor or magnetic NPs) of hollow colloidal NPs endowed with diverse properties and multiple functionalities [2]. The vast majority of synthetic approaches toward yolk@*h*SiO$_2$ NPs, however, involve only a single-component yolk. Relatively little research effort has been devoted to the synthesis of metal–semiconductor yolk/shell nanostructures [33]. Herein, we have synthesized, for the first time, a dual-yolk/shell nanostructure, comprising a semiconductor–metal hybrid nanocrystal dual-yolk within a hollow silica nanosphere.

Colloidal hybrid nanocrystals perform versatile functions and exhibit unique properties because they combine disparate material systems, such as semi-conductors and metals, semiconductors and metal oxides, and metal oxides and metals [34, 35]. A number of synthetic methods have been reported that allow control over the size, shape, and composition of hybrid nanocrystals, including selective anisotropic growth [36], formation of micelles [37], oxidation-directed decomposition [38], Ostwald ripening [39], and phase-transfer protocols [40]. In this study, we used a silica etching process locally accelerated by aurate hydroxyl complexes [Au(OH)$_4^-$] to synthesize CdSe/CdS/ZnS core–shell–shell quantum dot (CSSQD)–Au hybrid nanocrystals (CSSQD–Au) *in situ* in hollow silica nanostructures (Fig. 1). Notably, water-soluble poly-*L*-histidine-coated CSSQD@SiO$_2$ core/shell NPs (CSSQD@SiO$_2$–PLH) prevented the outer silica surfaces from being etched; the resultant etching procedure to form the yolk/shell nanostructures required only 10 min, implying the existence of a unique etching driving force that resulted in high etching rates within the silica shell. On the basis of our results, we suspect that during the reduction of Au ions proximal to the CSSQDs, liberation of OH$^-$ ions from Au(OH)$_4^-$ led to an increase the local pH. Such QD/metal hybrid nanocrystals spatially nanoconfined within permeable silica hollow nanospheres, thereby provide recyclability and potential opportunities for improving the electrical
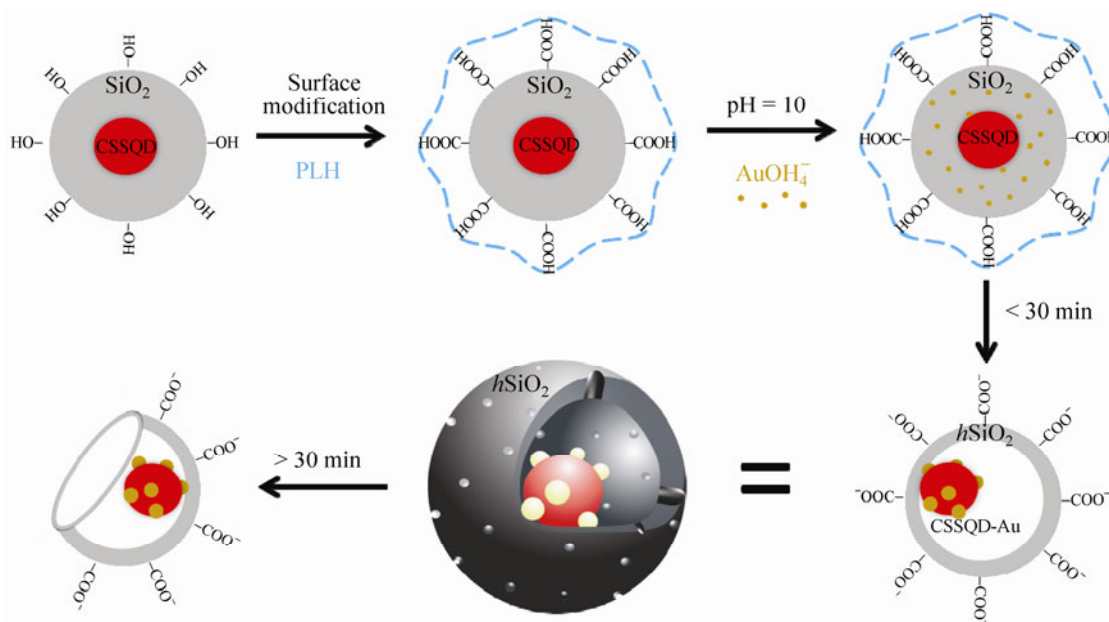

Figure 1 Schematic representation of the preparation of CSSQD–Au hybrid nanocrystal–SiO$_2$ yolk/shell nanocapsules

[41], biological [42], photocatalytic [43–45], and solar energy [46] applications based on light-induced electron transfer from the QD to the metal [36].

2. Results and discussion

Figure 2 shows transmission electron microscopy (TEM) images of CdSe QDs and CdSe/CdS/ZnS CCSQDs. Monodisperse CdSe QDs (5.2 nm ± 0.3 nm; photoluminescence (PL) emission: 595 nm) were synthesized using a general method [47]; CdSe/CdS/ZnS core/shell/shell QDs (CSSQDs; average size: 10.1 nm ± 1.0 nm; PL emission: 653 nm) were synthesized using a successive ion layer adhesion and reaction (SILAR) method [48]. CSSQD@SiO$_2$ core/shell NPs (CSSQD@SiO$_2$–OH) were prepared in non-ionic reverse microemulsions [49]. 3-Aminopropyltriethoxysilane (APTMS) and succinic anhydride were used successively to transform the surface of the CSSQD@SiO$_2$–OH particles first into amino-functionalized (CSSQD@SiO$_2$–NH$_2$) and then into carboxylic acid–functionalized silica (CSSQD@SiO$_2$–COOH) [50]. To increase the solubility in water and protect the silica surface from alkaline etching, the CSSQD@SiO$_2$–COOH particles were further coated with poly-*L*-histidine (CSSQD@SiO$_2$–PLH) [51].

As shown in Fig. 3(a), the TEM image revealed that the resulting CSSQD@SiO$_2$–PLH particles were nearly spherical, with an average diameter of 42.5 nm ± 4.2 nm. A single CSSQD–Au hybrid nanocrystal decorated within hSiO$_2$ was prepared using the following rapid and simple process. 4 mL of aqueous hydrogen tetrachloride aurate (Ⅲ) (HAuCl$_4$; 0.0005 mol/L) was
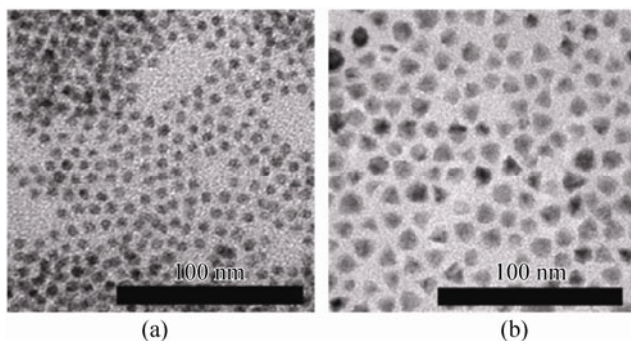

Figure 2 TEM images of (a) CdSe and (b) the CdSe/CdS/ZnS CSSQDs
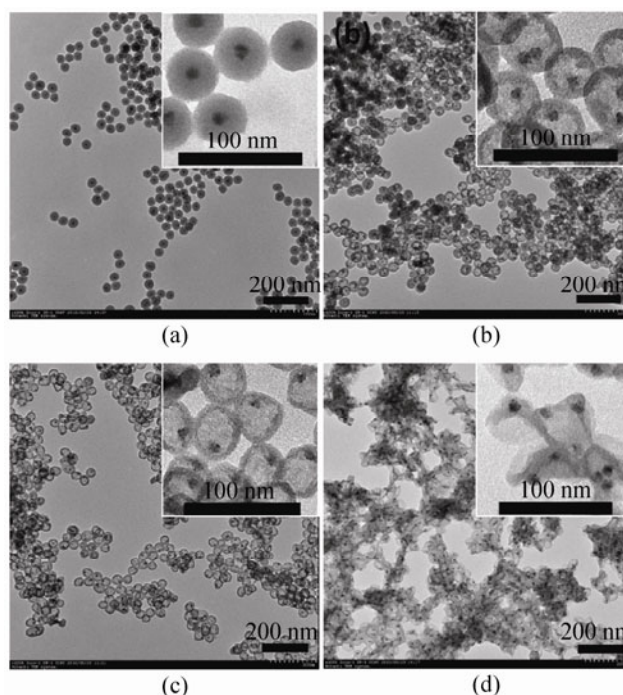

Figure 3 TEM images of CSSQD–Au@SiO$_2$ NPs (a) before etching and after etching for (b) 10, (c) 20, (d) 50 min

adjusted to pH 10 using 1 mol/L NaOH, forming a colorless HAuCl$_4$/NaOH solution as a result of the formation of Au(OH)$_4^-$ ions [52]. After incubating 100 μL of CCSQD@SiO$_2$–PLH core/shell NPs (1 μmol/L) in the aqueous Au(OH)$_4^-$ solution, the mixture was centrifuged (12 000 rpm) to collect the resultant NPs and remove any unreacted ions.

TEM images of the monodisperse CSSQD@SiO$_2$–PLH after Au(OH)$_4^-$ etching (Figs. 3(b)–3(d)) indicated the evolution of the formation of the CSSQD–Au hybrid nanocrystal–hollow SiO$_2$ yolk/shell nanostructure (CSSQD–Au@hSiO$_2$) as a function of increasing etching time. Most interestingly, the CSSQD–Au@hSiO$_2$ yolk/shell NPs were formed rapidly, by incubating in aqueous Au(OH)$_4^-$ solution for only 10 min (Fig. 3(b)). This procedure is not only the most rapid method for producing silica-based yolk/shell NPs but also the first time the *in situ* synthesis of QD–metal hybrid nanocrystals encapsulated within silica hollow structures has been reported. Furthermore, the thickness of the hSiO$_2$ changed from 10.3 nm ± 2.1 nm (Fig. 3(b)) to 7.0 nm ± 1.5 nm (Fig. 3(c)) upon increasing the incubation time in the aqueous HAuCl$_4$/NaOH solution from 10 to 20 min. For etching times greater

than 30 min, the hollow SiO_2 nanospheres became elliptical, sunken, and eventually broken (Fig. 3(d)). The tunable thickness, controlled by varying the etching time, altered the volume of the void space between the CSSQD–Au dual-yolk and the $hSiO_2$ shell; the thickness of the $hSiO_2$ shell was limited, however, by the stability of the shell architecture. Moreover, the scanning electron microscopy (SEM) image of the CSSQD@SiO_2 NPs in Fig. 4(a) also reveals their well-controlled shapes and narrow size distribution. The SEM image of the products obtained after etching for 20 min (Fig. 4(b)) reveals that some of the NPs possessed openings and cavities, supporting the formation of hollow SiO_2 particles.

Because TEM and SEM analyses are performed under vacuum, they require dry samples; therefore, we also examined the evolution of the formation of the yolk/shell nanostructures in solution using small-angle X-ray scattering (SAXS; Fig. 5). The core/shell model fitting profile (red dashed line) fits well to the SAXS profile of the CSSQD@SiO_2–PLH core/shell NPs, indicating that the core/shell nanoarchitecture (shown schematically in the inset) of the CSSQD@SiO_2 NPs was well defined. The overall diameter of the CSSQD@SiO_2 core/shell nanostructure and the diameter of the CSSQD core were 44 and 10 nm, respectively [53], similar to the sizes measured using TEM. After etching for 10 and 20 min, the first peak became less intense than the second, revealing that the scattering of the silica shell decreased as a result of the inside-out formation of empty space from the interface between the SiO_2 shell and the CSSQD core (i.e. a rolling core
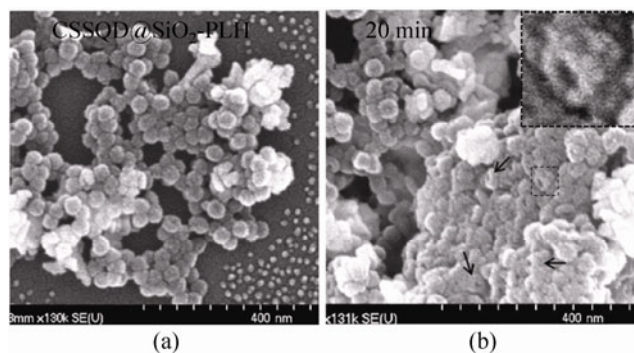

Figure 5   Ex situ solution SAXS profiles of CSSQD–Au@SiO_2 NPs prepared with etching times ranging from 0 to 60 min

formed inside a large empty Si shell). In addition, the shift of the two peaks to low wavevector transfer (Q) indicates a slight growth of the CSSQD core, most likely due to the attachment of small Au NPs (cf. the insets in Figs. 3(b) and 3(c)). The first peak become broader and more intense than the second after 30 min, suggesting that the polydispersity of the overall size of the CSSQD@$hSiO_2$ particles had decreased and that the deformation of CSSQD@$hSiO_2$ yolk/shell nanostructures was beginning. Finally, the damping of the second peak after 50 min reveals the loss of coherent structure between the SiO_2 shells and the CSSQD cores as a result of destruction of the yolk/shell nanostructures, consistent with our TEM observations (Fig. 3(d)). The coherence of our TEM, SEM, and SAXS observations confirms the evolution of the formation of the yolk/shell nanostructures during the inside-out etching procedure.

In the TEM images in Fig. 6(a), a few dark spots with enhanced contrast attached to the CSSQD surfaces were observed, suggesting a different material with high electron density. Using energy-dispersive X-ray (EDX) spectroscopy (Figs. 6(b) and 6(c)), selected-area EDX elemental analysis confirmed that the yolk was both Cd-rich (CSSQD) and Au-rich (Au nanoclusters), while the shell was only Si-rich ($hSiO_2$). In addition, the EDX line scanning profiles indicated the locations of the Si, Cd, and Au elements in the yolk/shell

Figure 4   SEM images of CSSQD–Au@SiO_2 NPs (a) before and (b) after etching for 20 min. The arrows in (b) indicate open rings, a typical structural feature suggesting the presence of voids
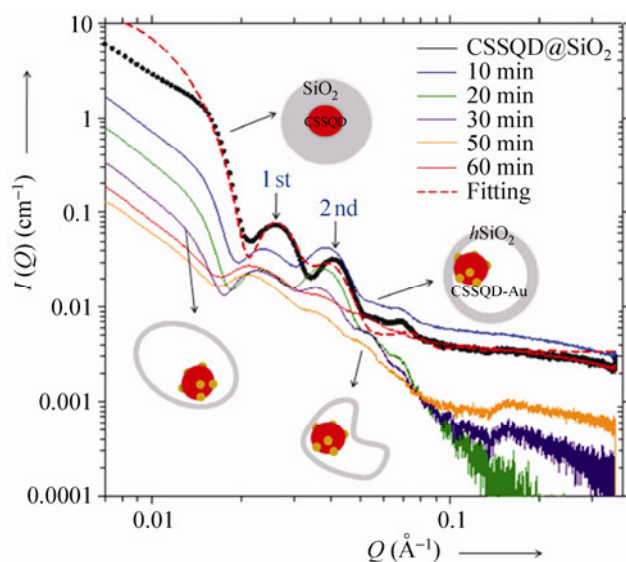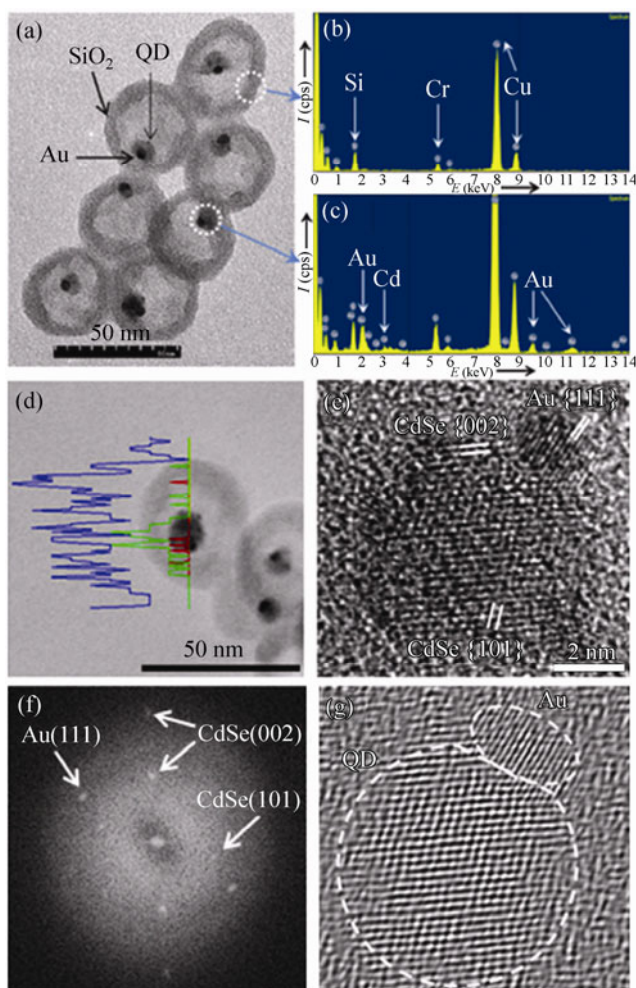
Figure 6 (a)–(c) TEM image and selected-area EDX elementary analysis of CSSQD–Au@hSiO$_2$ yolk/shell nanospheres. (d) STEM image and EDX elementary line scanning of the CSSQD–Au@hSiO$_2$ yolk/shell nanospheres. Blue, green, and red lines represent Si, Cd, and Au, respectively. (e) The HRTEM lattice image of a CSSQD–Au yolk and the corresponding lattice planes. (f) The FFT image of (e). (g) The inverse FFT image from (f)

nanostructure (Fig. 6(d)). The Cd- and Au-rich positions correspond to the locations of the CSSQD–Au spots observed using scanning transmission electron microscopy (STEM). The EDX and STEM analyses demonstrate the formation of a dual-yolk composed of CSSQD–Au hybrid nanocrystals encapsulated within hSiO$_2$.

Further evidence for this structure was provided by high-resolution TEM (HRTEM) analysis of the lattice image of a CSSQD–Au hybrid nanocrystal (Fig. 6(e)). The lattice spacings for the major NP and the attached NP were approximately 0.33 and 0.24 nm, respectively,

consistent with the (002) facet of CdSe and the (111) facet of Au, respectively. Accordingly, both EDX and HRTEM analysis confirmed that the yolk was a hybrid nanocrystal of CSSQD/Au.

The detailed interface between the CSSQD and Au NPs in the nanocluster was not clear because it was difficult to record the lattice images of both species simultaneously. The inverse fast Fourier transform (FFT) image (Fig. 6(f)), reconstructing the TEM image of CSSQD–Au hybrid nanocrystals (Fig. 6(g)) from the characteristic spots of the FFT image, revealed that the CSSQD–Au interface was disordered and discontinuous. Although recent reports suggest that the Au {111} facet should lie parallel to the wurtzite CdSe {101} facet [33, 35, 39], our CSSQD–Au hybrid nanocrystals did not feature such a phenomenon.

There are several factors that might explain this discrepancy. First, we used CdSe/CdS/ZnS CCSQDs in this study; natural lattice mismatch among CdSe, CdS, and ZnS might twist the {101} facet proximal to the outer surfaces. Second, the silica coating of the CSSQDs might have obstructed the CdSe {101} facet and affected Au attachment on the low-energy sites. Third, our synthetic approach and conditions are different from those employed in the previous studies. In our case, the QSSQD and Au precursor were in aqueous solution; we used aurate hydroxyl complexes without a reductant, whereas an organometallic Au^I complex with a reductant (e.g. ethylene glycol) was employed in the previous studies [35]. Together, these factors might explain the different priority facets of the CSSQDs for Au attachment.

To date, the formation of silica-based dual-yolk/shell structures has always involved a single-component yolk and has required incubation for a few hours, several days, or even a month. Our results reveal two unusual characteristics of the CSSQD–Au@SiO$_2$ dual-yolk/shell nanostructures: a yolk of binary hybrid nanocrystals, and rapid etching behavior involving CSSQD@SiO$_2$ core/shell NPs as template and aqueous alkaline Au(OH)$_4^-$ solution as etching agent. To understand the driving force behind the simultaneous rapid etching behavior and formation of CSSQD–Au dual-yolk, we performed two control experiments (Fig. 7)—different surface-modified SiO$_2$ NPs and the absence of Au(OH)$_4^-$—to determine the key to the formation of the CSSQD–Au@hSiO$_2$ dual-yolk/shell NPs.
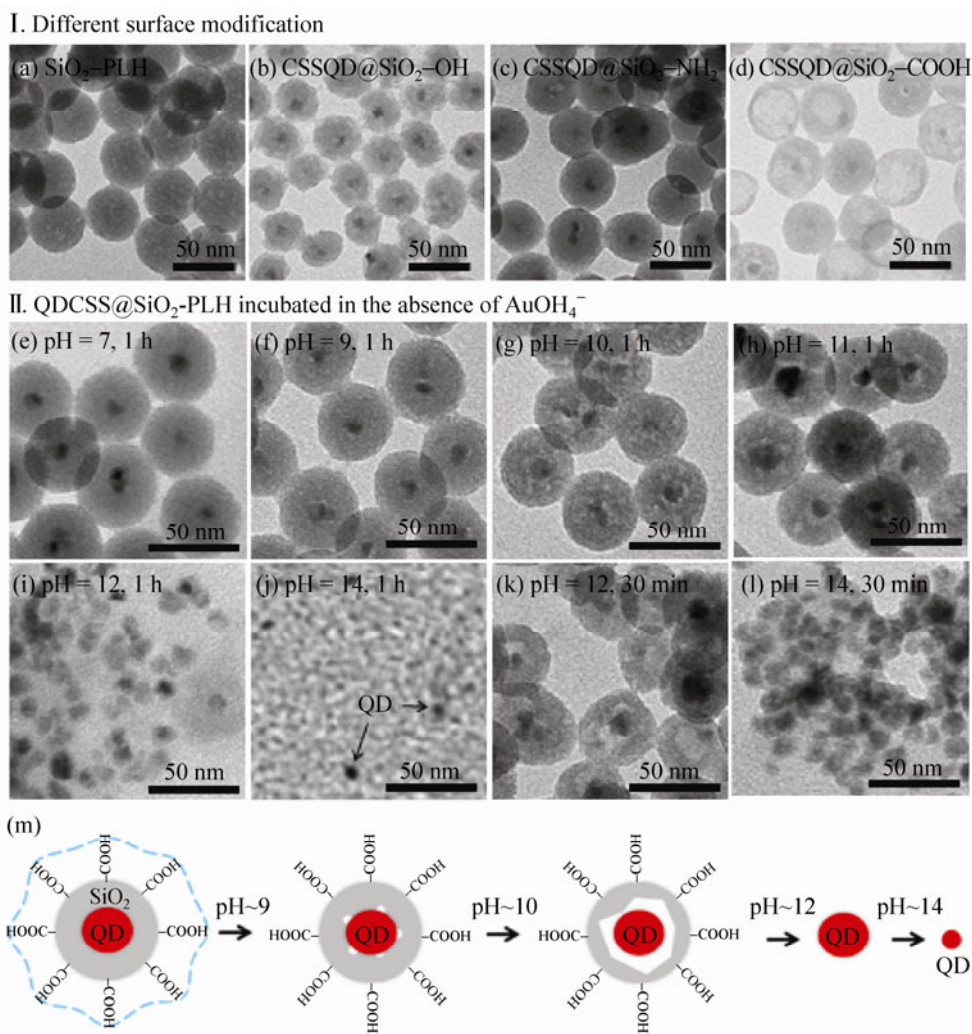
Figure 7 TEM images of different surface-modified SiO₂ and CSSQD/SiO₂ core/shell NPs after incubating in aqueous AuOH₄⁻ solutions for 20 min at pH 10. (a) SiO₂–PLH; (b) CSSQD@SiO₂–OH; (c) CSSQD@SiO₂–NH₂; (d) CSSQD@SiO₂–COOH. TEM images of CSSQD@SiO₂–PLH core/shell NPs obtained after incubation for 1 h in aqueous NaOH solutions (absence of HAuCl₄) at (e) pH 7, (f) pH 9, (g) pH 10, (h) pH 11, (i) pH 12, and (j) pH 14 and incubation for 30 min at (i) pH 12 and (g) pH 14. (m) Schematic representation of the etching of CSSQD/SiO₂ core/shell NPs in aqueous NaOH solutions of different pH

The TEM images of different surface-modified SiO₂ and CSSQD@SiO₂ core/shell NPs after etching for 20 min in aqueous Au(OH)₄⁻ solution at pH 10 are shown in Fig. 7. The image of SiO₂–PLH (Fig. 7(a)), without a CSSQD core, reveals a surface with good shape but with partial etching of pores within the silica particle. The different etching tendencies of SiO₂–PLH and CSSQD@SiO₂–PLH (Fig. 3(c)) imply that a core encapsulated within silica was necessary to generate a hollow structure, because the loose silica and ZnS layer close to the CSSQD–silica interface are readily hydrolyzed. In addition, the TEM image of the

non-surface modified SiO₂–OH (Fig. 7(b)) reveals the decreased size and damaged surface of these particles, indicating that the Au(OH)₄⁻ ions have similar catalytic ability to OH⁻ ions because of the low hydrolysis rate in the aqueous alkaline solution at pH 10. In contrast, the TEM image of the CSSQD@SiO₂–NH₂ after etching (Fig. 7(c)) reveals well-shaped outer silica surfaces with few etched pores within the silica shells. The selective etching phenomenon might derive from a "surface-protected etching" process. The etching of CSSQD@SiO₂–NH₂ was dissimilar to that of SiO₂–PLH, possibly because interactions between hydroxyl Au

ions and amino groups proximal to the silicon surface hindered the diffusion of the $Au(OH)_4^-$ ions into the silica. In addition, the $CSSQD@SiO_2–COOH$ particles (Fig. 7(d)) featured hybrid structures, with full, hollow, and partially hollow silica nanospheres. The uniform but rapid etching might have been due to the poor suspension of $CSSQD@SiO_2–COOH$ in water and the reduction of $Au(OH)_4^-$ within the silica shells. Notably, only the water-soluble polymer-protected $CSSQD@SiO_2–PLH$ particles (Fig. 3) could produce completely hollow silica nanospheres containing CSSQD–Au yolks through remarkably rapid etching. Therefore, a polymer coating layer or a silane with nonoxyl substituents surface-modified on the silica particles should be able to protect the superficial Si–O–Si bonds from etching by OH^- ions [29, 32]. Surface-protected selective etching confines the hydrolysis to within the interior of the silica particles. However, unlike general surface-protected selective etching methods, we observed the directional and rapid "inside out" etching reaction starting from the interface between CSSQD and SiO_2, implying there should be a driving force dominating the unexpected etching behavior.

The rate of hydrolysis of silica is typically controlled by the concentration of OH^- ions (or pH) or the temperature in the incubation solution. In our study, OH^- ions were liberated locally near the CSSQD–SiO_2 interfaces, while $Au(OH)_4^-$ ions were reduced by electrons via the low energy sites of the sulfide-terminated end (CdS and ZnS multilayers) for Au nucleation and the light-induced excitons (QD + $h\nu \rightarrow$ $h^+ + e^-$) on CSSQD [54, 55]. To clarify the proposed mechanism for the unexpectedly rapid etching of the $CSSQD@SiO_2–PLH$ particles with $OH^-/Au(OH)_4^-$ as the etching catalyst, we performed another control experiment using aqueous NaOH solutions with various values of pH (i.e. the absence of Au ions) to etch $CSSQD@SiO_2–PLH$. After etching for 1 h, we observed slow etching at values of pH of less than 11 (Figs. 7(e)–7(h)), with most of the initial etching pores proximal to the interface between the CSSQD particles. In contrast, silica shells were etched dramatically within 30–60 min at pH 12 or higher (Figs. 7(i)–7(l)). Figure 7(m) is a cartoon showing the etching morphologies under different pH conditions. Notably, however, uniform $CSSQD@SiO_2$ yolk/shell nanostructures were not produced through etching in aqueous NaOH in the absence of $Au(OH)_4^-$ ions, supporting the suggestion that the formation of hollow structures required $Au(OH)_4^-$ ions. In addition, the CSSQD particles were tolerant to aqueous solutions of pH 12 or lower for at least 1 h, despite the silica coating being entirely etched, because of the additional CdS layer coated on the CdSe cores; thus, CSSQD–Au hybrid nanocrystals could be synthesized during the etching process. $Au(OH)_4^-$ plays an important dual role in the yolk formation of the CSSQD/Au hybrid nanocrystals and in the remarkable etching behavior. Because $Au(OH)_4^-$ ions contains four OH^- ions, 0.0005 mol/L $Au(OH)_4^-$ is equivalent to 0.002 mol/L OH^-, namely pH 11.3. Although a pH of 11.3 was not enough to cause such rapid etching for $CSSQD/Au@SiO_2$ yolk/shell formation [56], the hydrolysis might have been further accelerated by (1) a loose interior silica structure, with hydroxyl-rich sites (Si–OH) adjacent to CSSQD surfaces, formed through the reverse microemulsion method; (2) the increased opportunity for collisions between OH^- ions [from $Au(OH)_4^-$ ions] and Si–O units, due to the nanoconfined domain proximally located to the CSSQD–SiO_2 interfaces; and (3) the local pH may be higher than 11.3, due to the rapid diffusion of $Au(OH)_4^-$ ions in silica resulting in the liberation of more and more OH^- ions after Au reduction. Therefore, the rate of silica hydrolysis at the CSSQD–SiO_2 interface was faster than theoretically expected, leading to the unexpectedly rapid etching.

The PL intensities of the CSSQD, $CSSQD@SiO_2–PLH$, and $CSSQD–Au@hSiO_2$ NPs decreased sequentially after coating with silica, further surface modification, and $Au(OH)_4^-$ etching (Fig. 8(a)). Quenching of the emission of CSSQDs presumably occurred as a result of the new nonradiative pathways created by the proximity of Au NPs, most likely from excited electrons transferring from the CSSQD NPs to the Au sites. Similarly, the fluorescence lifetime profiles of the CSSQD, $CSSQD@SiO_2–PLH$, and $CSSQD–Au@hSiO_2$ NPs (Fig. 8(b)) were obtained by time-correlated single photon counting (TCSPC) and the calculated fluorescence lifetimes were 23.54 ns ± 0.28 ns, 11.89 ns ± 0.13 ns,
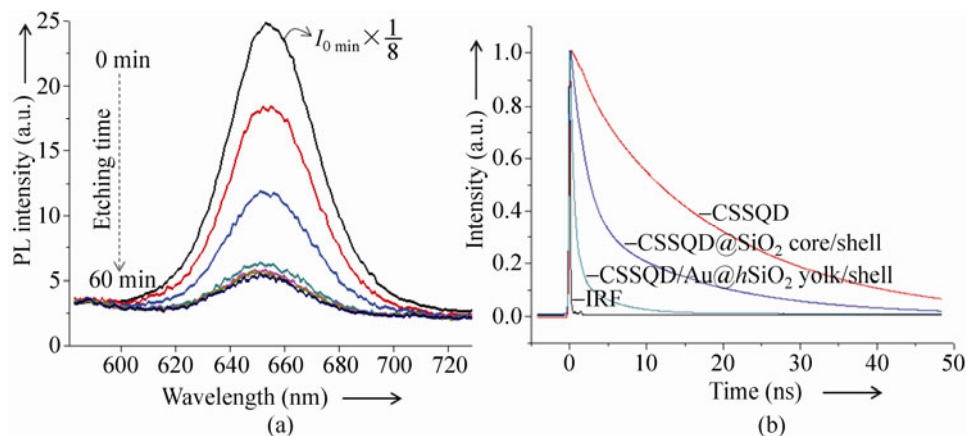
Figure 8 (a) *In situ* PL profiles of the formation of CSSQD–Au/silica hollow nanospheres. (b) Time-correlated single photon counting (TCSPC) profiles of the instrument response function (IRF), CSSQDs, CSSQD/SiO₂–PLH core/shell, and CSSQD–Au/hSiO₂ yolk/shell NPs

and 2.23 ns ± 0.11 ns, respectively. The apparent drop in the rate of fluorescence decay of the CSSQD–Au@SiO₂ NPs also illustrates that the electrons are almost all transferred to the Au NPs, resulting in a dramatic reduction in the quantum efficiency of the electron/hole recombination. Taking advantage of such metal-induced PL quenching, recent reports have described semiconductor/Au hybrid nanocrystals featuring a longer retention time of Au-trapping electrons and their potential application in photocatalytic reactions [36, 43]. Moreover, recent reports have shown how the electron transfer can also be used to grow Au NPs on QDs, because the Au centers are preferred sites for electron retention which helps to reduce additional Au ions [43, 55].

The size of the catalyst center (e.g. Au NPs) incorporated in the hollow silica nanospheres affects the catalyst efficiency [5, 37], and the permeable hollow silica shell must allow the reactant to pass through, but prevent the catalyst center from aggregating, during recycling through centrifugation or dialysis [5, 7, 29]. Therefore, as shown in Fig. 9(a), we have demonstrated that the sizes of the attached Au NPs can grow further using a photoreduction procedure, from a size dispersion of 1–1.5 nm (Fig. 9(b)) to 2–5 nm (Fig. 9(c)), upon exposure to UV light (312 nm, 3 mW) for 30 min in an additional aqueous aurate solution (pH 7). Accordingly, the recyclability of the CSSQD–Au@SiO₂ dual-yolk/shell nanomaterials and the tunable size

of the Au NPs make them suitable for catalytic application, especially as photocatalysts, because of charge generation via electron transfer from semiconductor nanocrystals. We believe our preliminary findings show yolk/shell nanomaterials can have diverse properties and multiple functionalities.
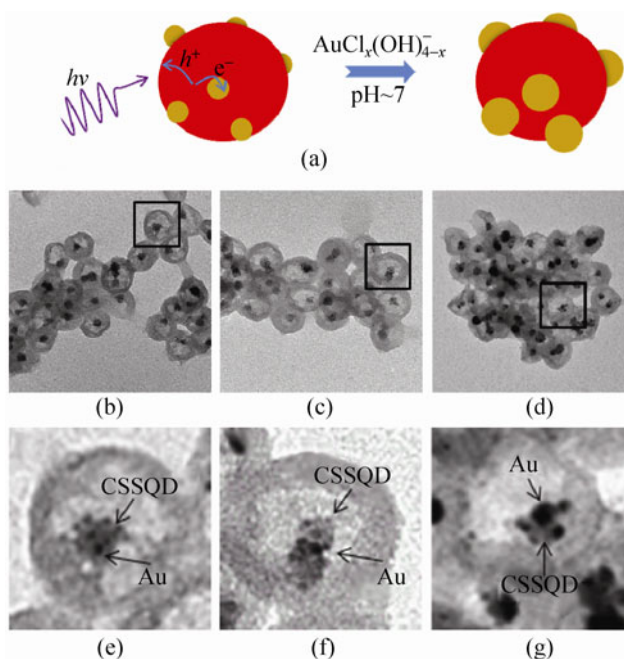

Figure 9 (a) Schematic representation of the mechanism of photoinduced growth of attached Au NPs on a CSSQD–Au hybrid nanocrystal. TEM images of CSSQD–Au@hSiO₂ (b, e) before UV exposure, (c, f) after incubating in aqueous aurate solution in the dark, and (d, g) after incubating in aqueous aurate solution and UV exposure

3. Conclusions

We have developed a versatile and rapid strategy for the synthesis of semiconductor–metal@hSiO$_2$ dual-yolk/shell NPs. The proposed mechanism of formation of semiconductor/metal dual-yolk and SiO$_2$ hollowness occurs through a localized hydroxyl-releasing strategy (via metal–hydroxyl complexes) and selectively accelerated etching (via silica surface modification). Au(OH)$_4^-$ anions raised the local pH proximal to the CdSe/CdS/ZnS CSSQD–Au interfaces during the reduction of Au ions by light-driven or Au-sulfide redox reactions; polymer-coated silica prevented the hydrolysis reaction from occurring on the silica surfaces. Moreover, the resulting platform offers a number of attractive features: (1) the most rapid and directional etching approach for the formation of hollow silica nanostructures in solution; (2) the formation of semiconductor/metal hybrid nanocrystals as yolks within hollow silica nanospheres for the first time; and (3) the ability, through light exposure, to tune the sizes of the attached metal nanoclusters on the encapsulated CSSQD within the hollow silica nanospheres. On the basis of this strategy, we suspect that the aurate hydroxyl complexes and the CdSe/CdS/ZnS CSSQDs could be tailored or replaced by other metal ions and other semiconductor QDs, respectively, potentially leading to many promising applications in fuel cells, photocatalysis, bioimaging, and cancer therapy.

4. Experimental

4.1 Materials

Tetraethoxysilane (TEOS), methanol, ammonium hydroxide (25%), and APTMS were purchased from Acros Organics. Gold (Ⅲ) chloride trihydrate (HAuCl$_4$·3H$_2$O), hexane, chloroform, acetone, NaOH, CdO powder, Se powder, sulfur, zinc oxide, oleic acid, 1-octadecene (ODE), trioctylphosphine oxide (TOPO), octadecylamine (ODA), tri-n-butylphosphine (TBP), Igepal CO-520, succinic anhydride, N,N-dimethylformamide (DMF), and poly-L-histidine (PLH) were obtained from Sigma-Aldrich Chemical Co.

4.2 Synthesis of CdSe QDs

CdSe nanocrystals were prepared using a modified literature procedure [47]. In a typical reaction, a mixture of CdO (0.4 mmol), oleic acid (1.6 mmol), and ODE (5 g) was heated in a 25-mL three-neck flask at ca. 200 °C to obtain a colorless clear solution. After cooling to room temperature, ODA (3 g) and TOPO (1 g) were added to the flask. Under an Ar flow, this system was further heated at 300 °C. At this temperature, a selenium stock solution, prepared from Se (2 mmol) and TBP (1 g) and further diluted with ODE (2.5 g), was rapidly injected. The temperature was maintained at 300 °C for the growth of CdSe nanocrystals. The reaction mixture was cooled by liquid N$_2$ to room temperature, and extraction with CHCl$_3$/MeOH (1:3, v/v) was used to purify the nanocrystals and remove any side products and unreacted precursors. The nanocrystals dissolved in the CHCl$_3$/ODE layer; excess amines and unreacted precursors were extracted into the MeOH layer. The resultant CdSe solution was dissolve in CHCl$_3$ and was used as a stock solution for the growth of the CdSe/CdS/ZnS CSSQDs.

4.3 Synthesis of CdSe/CdS/ZnS CSSQDs using the SILAR method

Multishell CdSe QDs were synthesized using a SILAR method [48]. CdSe nanocrystals (diameter: 5.2 nm; 10^{-4} mmol of particles, in CHCl$_3$) were mixed with ODA (7.5 g) and ODE (25 g) in a 50-mL three-neck flask. The CHCl$_3$ in the flask was pumped out using a mechanical pump (room temperature, 30 min) and then residual air from the system was removed under an Ar flow at 100 °C (5–10 min). Subsequently, the reaction mixture was heated at 240 °C before the injection of the shell stock solution. The concentrations of the shell stock solution for the Cd/oleic acid/ODE, S/ODE, and Zn/oleic acid/ODE shells were 0.04 mol/L. The amount of shell stock solutions injected for each layer were as follows: (1) first CdS layer, 0.86 mL of the Cd and S stock solutions; (2) second CdS layer, 0.59 mL of the Cd and S stock solutions; (3) third Cd$_{0.75}$Zn$_{0.25}$S layer, 0.92, 0.31, and 1.22 mL of the Cd, Zn, and S stock solutions, respectively; (4) fourth

$Cd_{0.5}Zn_{0.5}S$ layer, 0.73, 0.73, and 1.46 mL of the Cd, Zn, and S stock solutions, respectively; (5) fifth $Cd_{0.25}Zn_{0.75}S$ layer, 0.43, 1.29, and 1.72 mL of the Cd, Zn, and S stock solutions, respectively; (6) sixth ZnS layer, 1.98 mL of the Zn and S stock solutions; and (7) seventh ZnS layer, 2.30 mL of the Zn and S stock solutions. The shell stock solutions were not added in a dropwise manner; instead, 0.1 mL of each solution was injected in less than 1 s. The reaction was terminated by allowing the mixture to cool. The resulting nano-crystals (Fig. 2(b)) were precipitated by adding acetone into the $CHCl_3$ solution. Excess amines were further removed by dissolving the nanocrystals in $CHCl_3$ and precipitating them with acetone.

4.4 Synthesis of CSSQD@SiO2–OH using a reverse microemulsion method

Silica-coated QD nanoparticles were synthesized by using a reverse microemulsion method [49]. Typically, cyclohexane (4.38 mL), Igepal CO-520 (0.225 mL), CSSQDs (10^{-6} mol/L, 50 μL) stock solution in $CHCl_3$, and TEOS [$Si(OEt)_4$, 30 μL] were added to a flask under vigorous stirring for 30 min. Aqueous ammonia (25 wt.%, 100 μL) was introduced to initiate the silica condensation process. The silica growth was com-pleted after 18 h of stirring at room temperature. Excess reactants were removed by dissolving and centrifuging the NPs in EtOH.

4.5 APTMS-modified CSSQD@SiO2 NP surfaces (CSSQD@SiO2–NH2)

An excess of APTMS (50 μL, 0.28 mmol) was added to a CSSQD@SiO2 NP/EtOH solution (10^{-7} mol/L, 5 mL) and left to react for 2 h. To enhance the covalent bonding of the APTMS groups to the silica surface, the solution was heated under a gentle reflux for an additional 1 h. The CSSQD@SiO2–NH2 NPs were washed by centrifuging and redispersing in EtOH.

4.6 Carboxylic acid–modified CSSQD@SiO2-NH2 NP surfaces (CSSQD@SiO2–COOH)

Succinic anhydride was used to further modify CSSQD@SiO2–NH2 to give CSSQD@SiO2–COOH [50]. A dispersion of CSSQD@SiO2–NH2 (10^{-7} mol/L, 5 mL) in dry DMF was prepared by centrifuging a dispersion

of CSSQD@SiO2–NH2 in EtOH, redispersing in EtOH/DMF (1:1), and then centrifuging and redispersing three times in DMF. The colloidal dispersion was opaque due to the poor solubility of the CSSQD@SiO2–NH2 NPs in DMF. An excess of succinic anhydride (100 mg) was added to the CSSQD@SiO2–NH2/DMF solution and left to stir overnight. The resulting solution became clear, indicating the carboxylic modification was successful. Excess succinic anhydride was removed through centrifugation and redispersion of the particles in DMF; this CSSQD@SiO2–COOH process was repeated three times. The CSSQD@SiO2–COOH NPs were finally redispersed in water by slowly increasing the ratio of H_2O to DMF. The increase in the DMF/H_2O ratio (*v/v* from 1:1, 3:1, to DMF only) was accompanied by an increase in opaqueness of the CSSQD@SiO2–COOH colloidal dispersion.

4.7 PLH–modified CSSQD@SiO2-COOH NP surfaces (CSSQD@SiO2–PLH)

PLH will adsorb onto the CSSQD@SiO2–COOH surfaces by electrostatic interaction [51]. PLH (3 mg) was added in a dispersion of CSSQD@SiO2–COOH (10^{-7} mol/L, 3 mL) in deionized (DI) water. The mixture of CSSQD@SiO2–COOH and PLH was gently stirred at room temperature for 2 h and unattached PLH removed by centrifugation (12 000 rpm) twice. The resultant CSSQD@SiO2–PLH was kept in a 4 °C fridge before use.

4.8 The etching process without Au

The nanoparticles used in our control experiments were incubated in aqueous solutions with pH 9, pH 10, pH 11, and pH 12 which were adjusted by using 1 N NaOH. After incubating for the required time, the resulting nanoparticles were centrifuged (12 000 rpm) and washed twice by DI water before characterization.

4.9 Characterization

TEM was performed using a Hitachi H-6500 instru-ment operated at 100 kV (for higher-contrast images) or a JEOL 2100 field-emission STEM instrument operated at 200 kV (for high-resolution images and EDX analysis). For TEM sample preparation, the NP solutions were deposited directly onto carbon-coated

copper grids. SAXS measurements were performed at the SWAXS endstation of the BL23A beamline of the Synchrotron Radiation Research Center (NSRRC). The details of this instrument have been reported previously [53]. With a 0.5-mm-diameter beam having a wavelength (λ) of 1.24 Å (10 keV) and a sample-to-detector distance of 2.4 m, SAXS data were collected in the wavevector transfer Q range from 0.007 to 0.25 Å^{-1}, which covered the scattering characteristics of the NPs. Here, Q was determined using the expression $4\pi\sin(\theta)/\lambda$ in terms of the scattering angle (2θ) and the wavelength of the X-rays (λ). The typical solution sample size for SAXS was a cylinder having dimensions of ca. (3 mm × 3 mm) × 0.5 mm. All of the SAXS data collected with an area detector were corrected for sample transmission, background, and the detector sensitivity; the value of Q was calibrated using silver behenate. Time-resolved intensity decays were recorded using a homemade TCSPC fluorescence lifetime spectrometer. The excitation at 488 nm was measured using a pulsed laser diode with a repetition rate of 20 MHz. The instrument response function (IRF) was ca. 300 ps in this TCSPC system. The excitation was vertically polarized and the emission was recorded through a polarizer oriented at 54.7° from the vertical position. A cut filter at 600 nm (Chroma) was used in the collection path to record the fluorescence from the QD multishell NPs. A two-component model was used to fit the fluorescence decay profiles.

Acknowledgements

References

[1] Yin, Y. D.; Rioux, R. M.; Erdonmez, C. K.; Hughes, S.; Somorjai, G. A.; Alivisatos, A. P. Formation of hollow nanocrystals through the nanoscale Kirkendall effect. *Science* **2004**, *304*, 711–714.

[2] Lou, X. W.; Archer, L. A.; Yang, Z. C. Hollow micro-/nanostructures: Synthesis and applications. *Adv. Mater.* **2008**, *20*, 3987–4019.

[3] Cheng, K.; Sun, S. H. Recent advances in syntheses and therapeutic applications of multifunctional porous hollow nanoparticles. *Nano Today* **2010**, *5*, 183–196.

[4] Ikeda, S.; Ishino, S.; Harada, T.; Okamoto, N.; Sakata, T.; Mori, H.; Kuwabata, S.; Torimoto, T.; Matsumura, M. Ligand-free platinum nanoparticles encapsulated in a hollow porous carbon shell as a highly active heterogeneous hydrogenation catalyst. *Angew. Chem. Int. Ed.* **2006**, *45*, 7063–7066.

[5] Lee, J.; Park, J. C.; Song, H. A nanoreactor framework of a Au@SiO$_2$ yolk/shell structure for catalytic reduction of *p*-nitrophenol. *Adv. Mater.* **2008**, *20*, 1523–1528.

[6] Chen, Z.; Cui, Z. M.; Niu, F.; Jiang, L.; Song, W. G. Pd nanoparticles in silica hollow spheres with mesoporous walls: A nanoreactor with extremely high activity. *Chem. Commun.* **2010**, *46*, 6524–6526.

[7] Park, J. C.; Bang, J. U.; Lee, J.; Ko, C. H.; Song, H. Ni@SiO$_2$ yolk–shell nanoreactor catalysts: High temperature stability and recyclability. *J. Mater. Chem.* **2010**, *20*, 1239–1246.

[8] Park, J. C.; Lee, H. J.; Kim, J. Y.; Park, K. H.; Song, H. Catalytic hydrogen transfer of ketones over Ni@SiO$_2$ yolk–shell nanocatalysts with tiny metal cores. *J. Phys. Chem. C* **2010**, *114*, 6381–6388.

[9] Wu, S. H.; Tseng, C. T.; Lin, Y. S.; Lin, C. H.; Hung, Y.; Mou, C. Y. Catalytic nano-rattle of Au@hollow silica: Towards a poison-resistant nanocatalyst. *J. Mater. Chem.* **2011**, *21*, 789–794.

[10] Gao, J. H.; Liang, G. L.; Zhang, B.; Kuang, Y.; Zhang, X. X.; Xu, B. FePt@CoS$_2$ yolk–shell nanocrystals as a potent agent to kill HeLa cells. *J. Am. Chem. Soc.* **2007**, *129*, 1428–1433.

[11] Gao, J. H.; Liang, G. L.; Cheung, J. S.; Pan, Y.; Kuang, Y.; Zhao, F.; Zhang, B.; Zhang, X. X.; Wu, E. X.; Xu, B. Multifunctional yolk–shell nanoparticles: A potential MRI contrast and anticancer agent. *J. Am. Chem. Soc.* **2008**, *130*, 11828–11833.

[12] Zhao, W. R.; Chen, H. R.; Li, Y. S.; Li, L.; Lang, M. D.; Shi, J. L. Uniform rattle-type hollow magnetic mesoporous spheres as drug delivery carriers and their sustained-release property. *Adv. Funct. Mater.* **2008**, *18*, 2780–2788.

[13] Li, L. L.; Tang, F. Q.; Liu, H. Y.; Liu, T. L.; Hao, N. J.; Chen, D.; Teng, X.; He, J. Q. *In vivo* delivery of silica nanorattle encapsulated Docetaxel for liver cancer therapy with low toxicity and high efficacy. *ACS Nano* **2010**, *4*, 6874–6882.

[14] Lu, Y.; Zhao, Y.; Yu, L.; Dong, L.; Shi, C.; Hu, M. J.; Xu, Y. J.; Wen, L. P.; Yu, S. H. Hydrophilic Co@Au yolk/shell nanospheres: Synthesis, assembly, and application to gene delivery. *Adv. Mater.* **2010**, *22*, 1407–1411.

[15] Zhu, Y. F.; Ikoma, T.; Hanagata, N.; Kaskel, S. Rattle-type $Fe_3O_4@SiO_2$ hollow mesoporous spheres as carriers for drug delivery. *Small* **2010**, *6*, 471–478.

[16] Hu, S. H.; Chen, Y. Y.; Liu, T. C.; Tung, T. H.; Liu, D. M.; Chen, S. Y. Remotely nano-rupturable yolk/shell capsules for magnetically-triggered drug release. *Chem. Commun.* **2011**, *47*, 1776–1778.

[17] Liu, H. Y.; Chen, D.; Li, L. L.; Liu, T. L.; Tan, L. F.; Wu, X. L.; Tang, F. Q. Multifunctional gold nanoshells on silica nanorattles: A platform for the combination of photothermal therapy and chemotherapy with low systemic toxicity. *Angew. Chem., Int. Ed.* **2011**, *50*, 891–895.

[18] Park, J. C.; Song, H. Metal@silica yolk–shell nanostructures as versatile bifunctional nanocatalysts. *Nano Res.* **2011**, *4*, 33–49.

[19] Wang, T. T.; Chai, F.; Wang, C. G.; Li, L.; Liu, H. Y.; Zhang, L. Y.; Su, Z. M.; Liao, Y. Fluorescent hollow/rattle-type mesoporous Au@SiO_2 nanocapsules for drug delivery and fluorescence imaging of cancer cells. *J. Colloid Interf. Sci.* **2011**, *358*, 109–115.

[20] Ha, T. L.; Shin, J.; Lim, C. W.; Lee, I. S. Seed-mediated growth of gold inside hollow silica nanospheres for sensing peroxide and glucose concentrations. *Chem-Asian J.* **2012**, *7*, 36–39.

[21] Lee, K. T.; Jung, Y. S.; Oh, S. M. Synthesis of tin-encapsulated spherical hollow carbon for anode material in lithium secondary batteries. *J. Am. Chem. Soc.* **2003**, *125*, 5652–5653.

[22] Zhang, W. M.; Hu, J. S.; Guo, Y. G.; Zheng, S. F.; Zhong, L. S.; Song, W. G.; Wan, L. J. Tin-nanoparticles encapsulated in elastic hollow carbon spheres for high-performance anode material in lithium-ion batteries. *Adv. Mater.* **2008**, *20*, 1160–1165.

[23] Zhang, Q.; Wang, W. S.; Goebl, J.; Yin, Y. D. Self-templated synthesis of hollow nanostructures. *Nano Today* **2009**, *4*, 494–507.

[24] Wu, X. J.; Xu, D. S. Formation of yolk/SiO_2 shell structures using surfactant mixtures as template. *J. Am. Chem. Soc.* **2009**, *131*, 2774–2775.

[25] Wu, X. J.; Xu, D. S. Soft template synthesis of yolk/silica shell particles. *Adv. Mater.* **2010**, *22*, 1516–1520.

[26] Park, S. J.; Kim, Y. J.; Park, S. J. Size-dependent shape evolution of silica nanoparticles into hollow structures. *Langmuir* **2008**, *24*, 12134–12137.

[27] Zhang, T. R.; Ge, J. P.; Hu, Y. X.; Zhang, Q.; Aloni, S.; Yin, Y. D. Formation of hollow silica colloids through a spontaneous dissolution–regrowth process. *Angew. Chem., Int. Ed.* **2008**, *47*, 5806–5811.

[28] Chen, D.; Li, L. L.; Tang, F. Q.; Qi, S. O. Facile and scalable synthesis of tailored silica "nanorattle" structures. *Adv. Mater.* **2009**, *21*, 3804–3807.

[29] Zhang, Q.; Zhang, T. R.; Ge, J. P.; Yin, Y. D. Permeable silica shell through surface-protected etching. *Nano Lett.* **2008**, *8*, 2867–2871.

[30] Zhang, Q.; Ge, J. P.; Goebl, J.; Hu, Y. X.; Lu, Z. D.; Yin, Y. D. Rattle-type silica colloidal particles prepared by a surface-protected etching process. *Nano Res.* **2009**, *2*, 583–591.

[31] Zhang, Q.; Lee, I.; Ge, J. P.; Zaera, F.; Yin, Y. D. Surface-protected etching of mesoporous oxide shells for the stabilization of metal nanocatalysts. *Adv. Funct. Mater.* **2010**, *20*, 2201–2214.

[32] Chen, Y.; Chen, H. R.; Guo, L. M.; He, Q. J.; Chen, F.; Zhou, J.; Feng, J. W.; Shi, J. L. Hollow/rattle-type mesoporous nanostructures by a structural difference-based selective etching strategy. *ACS Nano* **2010**, *4*, 529–539.

[33] Yang, J.; Peng, J. J.; Zhang, Q. B.; Peng, F.; Wang, H. J.; Yu, H. One-step synthesis and characterization of gold–hollow PbS_x hybrid nanoparticles. *Angew. Chem. Int. Ed.* **2009**, *48*, 3991–3995.

[34] Costi, R.; Saunders, A. E.; Banin, U. Colloidal hybrid nanostructures: A new type of functional materials. *Angew. Chem. Int. Ed.* **2010**, *49*, 4878–4897.

[35] Zeng, J.; Huang, J. L.; Liu, C.; Wu, C. H.; Lin, Y.; Wang, X. P.; Zhang, S. Y.; Hou, J. G.; Xia, Y. N. Gold-based hybrid nanocrystals through heterogeneous nucleation and growth. *Adv. Mater.* **2010**, *22*, 1936–1940.

[36] Dukovic, G.; Merkle, M. G.; Nelson, J. H.; Hughes, S. M.; Alivisatos, A. P. Photodeposition of Pt on colloidal CdS and CdSe/CdS semiconductor nanostructures. *Adv. Mater.* **2008**, *20*, 4306–4311.

[37] Tan, L. F.; Chen, D.; Liu, H. Y.; Tang, F. Q. A silica nanorattle with a mesoporous shell: An ideal nanoreactor for the preparation of tunable gold cores. *Adv. Mater.* **2010**, *22*, 4885–4889.

[38] Shi, W. L.; Zeng, H.; Sahoo, Y.; Ohulchanskyy, T. Y.; Ding, Y.; Wang, Z. L.; Swihart, M.; Prasad, P. N. A general approach to binary and ternary hybrid nanocrystals. *Nano Lett.* **2006**, *6*, 875–881.

[39] Mokari, T.; Sztrum, C. G.; Salant, A.; Rabani, E.; Banin, U. Formation of asymmetric one-sided metal-tipped semiconductor nanocrystal dots and rods. *Nat. Mater.* **2005**, *4*, 855–863.

[40] Yang, J.; Ying, J. Y. A General phase-transfer protocol for metal ions and its application in nanocrystal synthesis. *Nat. Mater.* **2009**, *8*, 683–689.

[41] Steiner, D.; Mokari, T.; Banin, U.; Millo, O. Electronic structure of metal–semiconductor nanojunctions in gold CdSe nanodumbbells. *Phys. Rev. Lett.* **2005**, *95*, 056805.

[42] Selvan, S. T.; Patra, P. K.; Ang, C. Y.; Ying, J. Y. Synthesis of silica-coated semiconductor and magnetic quantum dots and their use in the imaging of live cells. *Angew. Chem. Int. Ed.* **2007**, *46*, 2448–2452.

[43] Costi, R.; Saunders, A. E.; Elmalem, E.; Salant, A.; Banin, U. Visible light-induced charge retention and photocatalysis with hybrid CdSe–Au nanodumbbells. *Nano Lett.* **2008**, *8*, 637–641.

[44] Elmalem, E.; Saunders, A. E.; Costi, R.; Salant, A.; Banin, U. Growth of photocatalytic CdSe–Pt nanorods and nanonets. *Adv. Mater.* **2008**, *20*, 4312–4317.

[45] Gao, B.; Lin, Y.; Wei, S. J.; Zeng, J.; Liao, Y.; Chen, L. G.; Goldfeld, D.; Wang, X. P.; Luo, Y.; Dong, Z. C., et al. Charge transfer and retention in directly coupled Au–CdSe nanohybrids. *Nano Res.* **2012**, 5, 88–98.

[46] Tada, H.; Mitsui, T.; Kiyonaga, T.; Akita, T.; Tanaka, K. All-solid-state Z-scheme in CdS–Au–TiO$_2$ three-component nanojunction system. *Nat. Mater.* **2006**, *5*, 4782–4786.

[47] Qu, L. H.; Peng, X. G. Control of photoluminescence properties of CdSe nanocrystals in growth. *J. Am. Chem. Soc.* **2002**, *124*, 2049–2055.

[48] Li, J. J.; Wang, Y. A.; Guo, W. Z.; Keay, J. C.; Mishima, T. D.; Johnson, M. B.; Peng, X. G. Large-scale synthesis of nearly monodisperse CdSe/CdS core/shell nanocrystals using air-stable reagents via successive ion layer adsorption and reaction. *J. Am. Chem. Soc.* **2003**, *125*, 12567–12575.

[49] Zhang, B. B.; Gong, X. Q.; Hao, L. J.; Cheng, J.; Han, Y.; Chang, J. A novel method to enhance quantum yield of silica-coated quantum dots for biodetection. *Nanotechnology* **2008**, *19*, 465604.

[50] Mahalingam, V.; Onclin, S.; Peter, M.; Ravoo, B. J.; Huskens, J.; Reinhoudt, D. N. Directed self-assembly of functionalized silica nanoparticles on molecular printboards through multivalent supramolecular interactions. *Langmuir* **2004**, *20*, 11756–11762.

[51] Jin, Y. D.; Gao, X. H. Plasmonic fluorescent quantum dots. *Nat. Nanotechnol.* **2009**, *4*, 571–576.

[52] Moreau, F.; Bond, G. C.; Taylor, A. O. Gold on titania catalysts for the oxidation of carbon monoxide: Control of pH during preparation with various gold contents. *J. Catal.* **2005**, *231*, 105–114.

[53] Huang, C. M.; Wei, K. H.; Jeng, U. S.; Liang, K. S. Structural evolution of poly(styrene-*b*-4-vinylpyridine) diblock copolymer/gold nanoparticle mixtures from solution to solid state. *Macromolecules* **2007**, *40*, 5067–5074.

[54] Saunders, A. E.; Popov, I.; Banin, U. Synthesis of hybrid CdS–Au colloidal nanostructures. *J. Phys. Chem. B* **2006**, *110*, 25421–25429.

[55] Carbone, L.; Jakab, A.; Khalavka, Y.; Sonnichsen, C. Light-controlled one-sided growth of large plasmonic gold domains on quantum rods observed on the single particle level. *Nano Lett.* **2009**, *9*, 3710–3714.

[56] Feng, Z. G.; Li, Y. S.; Niu, D. C.; Li, L.; Zhao, W. R.; Chen, H. R.; Li, L.; Gao, J. H.; Ruan, M. L.; Shi, J. L. A facile route to hollow nanospheres of mesoporous silica with tunable size. *Chem. Commun.* **2008**, 2629–2631.